Sensors & Actuators: B. Chemical 384 (2023) 133621

Contents lists available at ScienceDirect

Sensors and Actuators: B. Chemical

journal homepage: www.elsevier.com/locate/snb

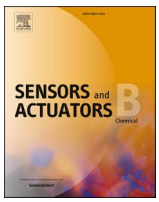

Electrochemical immunosensor utilizing a multifunctional 3D nanocomposite coating with antifouling capability for urinary bladder cancer diagnosis

R.K. Rakesh Kumar [a,1], Amit Kumar [a,1], Cheng-Hsin Chuang [a], Muhammad Omar Shaikh [b,*]

[a] Institute of Medical Science and Technology, National Sun Yat-sen University, Kaohsiung 80424, Taiwan
[b] Sustainability Science and Management Program, Tunghai University, Taichung 407224, Taiwan

ARTICLE INFO

Keywords:
Bladder cancer
Electrochemical immunosensor
3D nanocomposite
Antifouling
Point-of-care testing

ABSTRACT

Currently available point-of-care tests for Bladder Cancer (BC) are qualitative and prone to high false positives, thus preventing them from replacing clinical cystoscopy as reliable stand-alone diagnostics. In this study, we have targeted this unmet need by developing a label-free electrochemical impedimetric immunosensor for detection of APO-A1, a major high-density lipoprotein that is overexpressed in the urine of early-stage bladder cancer patients. The immunosensor utilizes a novel multifunctional 3D nanocomposite coating consisting of a porous bovine serum albumin (BSA) matrix embedded with a network of highly conductive and biocompatible gold coated silver nanowires (Au@AgNWs). The main components of this nanocomposite coating and their specific functions include: (i) A 3D porous BSA matrix to enable oriented antibody conjugation and prevent non-specific protein adsorption while allowing diffusion of analyte with minimal hindrance as compared to traditional antifouling coatings (ii) Embedded Au@AgNWs that enhance biocompatibility and improve charge transfer to the underlying electrode. The nanocomposite coating demonstrated minimal decrease in electrochemical performance even after 1-month of incubation in 1% BSA, human serum and human urine. Furthermore, the low-cost and disposable screen-printed electrochemical immunosensor exhibited excellent feasibility for sensitive and specific APO-A1 detection in the clinically relevant sensing range of 100 pg/mL to 250 ng/mL with high reproducibility (n = 5, RSD=2.2%) and an impressive LOD of 22 pg/mL. These results highlight the potential of the proposed immunosensor to enable reliable early diagnosis of bladder cancer at the point-of-care and serve as a viable alternative to cystoscopy.

1. Introduction

Globally, bladder cancer (BC) ranked among the top 10 common cancers in 2021 with 550,000 new cases annually and around 2.1% of all cancer related deaths [1,2]. Due to the high rate of recurrence and disease progression which requires regular long-term monitoring, BC confers the highest financial cost per patient amongst all malignancies in developed countries, with estimated costs of diagnosis and treatment in the United States ranging from $90,000 to $200,000 per patient and an annual overall cost of $3.4 billion [3]. BC can be categorized as either non-muscle-invasive bladder cancer (NMIBC) which has a low-risk of mortality or muscle-invasive bladder cancer (MBIC) which is potentially lethal in around 50% of patients with only a 5-year survival rate. If BC is detected and treated in the early stages (Grade 1), 95% of patients have shown to have a 5-year survival rate, which further highlights the need for reliable early diagnosis [4,5].

Currently, the gold standard for BC detection is cystoscopy which enables direct tumour visualization and tissue biopsy to confirm staging. Besides being invasive and painful for the patient, cystoscopy can suffer from low diagnostic accuracy, especially when detecting early-stage tumours which are missed in more than 20% of all cases [6]. Furthermore, the COVID-19 pandemic has had a worrying impact on proportions of patients waiting for cystoscopy in several developed countries. This has led the European Association of Urology (EAU) to issue new guidelines to deliver cystoscopy on a priority basis which further highlights the urgent need for developing non-invasive,

* Corresponding author.
E-mail address: omar@thu.edu.tw (M.O. Shaikh).
[1] R. K. Rakesh Kumar and Amit Kumar have equally contributed to the work.

https://doi.org/10.1016/j.snb.2023.133621
Received 18 December 2022; Received in revised form 22 February 2023; Accepted 5 March 2023
Available online 6 March 2023

affordable, and reliable diagnostic platforms that can enable point-of-care testing (POCT) of BC biomarkers directly using human urine samples [7]. At present, the FDA has approved five urinary tests for in vitro diagnostics (IVD) of BC which include BTA-Stat, BTA-TRAK, NMP22 BladderChek, UroVysion FISH and ImmunoCyt/uCyt+. While BTA-Stat and NMP22 BladderChek are suitable for POCT and demonstrate reasonable sensitivity for detecting advanced stage tumours, they are qualitative and unable to detect early-stage tumours with high specificity, thus resulting in false positive results [8,9]. Alternative tests like UroVysion FISH and ImmunoCyt are expensive and require trained professionals and well-equipped laboratories which limits their use in clinical practice [10,11]. Consequently, these FDA approved tests cannot be used as stand-alone diagnosis of BC and have only been utilized in conjunction with traditional cystoscopy and urine cytology. New emerging biomarkers are also being investigated and some of these demonstrate significantly higher sensitivity and specificity for early detection of BC as compared to cystoscopy, urine cytology and FDA approved urinary tests.

In particular, the detection of soluble urinary protein biomarkers using immunosensors is highly suitable for POCT of BC due to advantages like high specificity, rapid detection, widespread availability of complementary antibodies and ability to develop multiplexed assays for simultaneous detection of different biomarkers. Most reported immunosensors for BC utilize electrochemical transduction like Differential Pulse Voltammetry (DPV), Cyclic Voltammetry (CV) and Electrochemical Impedance Spectroscopy (EIS) while only a few have been reported using optical techniques like Fluorescence Resonance Energy Transfer (FRET) [12–15]. Electrochemical immunosensors are inherently more suited for label-free quantitative detection and have several advantages like simplicity, low-cost, reasonable sensitivity, and multiplexing capability due to ease of integration with miniaturized electronics, thus making them arguably the most suitable transduction scheme for POCT of proteins [16–18]. Furthermore, it is worthwhile noting that most studies generally focus on detection of typical BC biomarkers like BTA and NMP22 that have shown false positive results in patients with haematuria and other early-stage symptoms[19]. Only a few studies have been reported on novel investigational biomarkers like APO-A1 which have been clinically proven to have a higher sensitivity and specificity for early-stage BC detection [20,21].

Herein, we report on the development an electrochemical impedimetric immunosensor utilizing a novel multifunctional 3D nanocomposite coating for specifically targeting the unmet need of non-invasive POCT of BC as a viable alternative to clinical cystoscopy. The nanocomposite coating consists of a glutaraldehyde (GA) crosslinked porous bovine serum albumin (BSA) matrix embedded with a network of highly conductive and biocompatible gold coated silver nanowires (Au@AgNWs). This multifunctional coating not only allows oriented antibody immobilization and improved charge transfer but also reliable detection in complex fluids like urine owing to its in-built antifouling capability. The concentration of the nanocomposite components was optimized to achieve a uniform coating on the electrode surface with improved electrochemical performance. Finally, using the 3D nanocomposite modified screen-printed carbon electrode, we fabricated a highly sensitive and specific impedimetric immunosensor for detection of APO-A1 protein which is known to be clinically overexpressed in the urine of early-stage BC patients.

2. Materials and methods

2.1. Materials

Silver nitrate ($AgNO_3$, >99%), poly-vinylpyrrolidone (PVP, Mw 1300k), ethylene glycol (EG, 99.8% anhydrous), copper chloride hydrate ($CuCl_2.2H_2O$, >99%), hydrogen tetrachloroaurate trihydrate ($HAuCl_4.3H_2O$, 99.99%), sodium hydroxide (NaOH, >97%), sodium sulfite (Na_2SO_3, >98%), ascorbic acid ($C_6H_8O_6$, 99%), glutaraldehyde solution ($OHC(CH_2)_3CHO$, 25% in H_2O), ethylene glycol ($HOCH_2CH_2OH$, 99.8%), N-ethyl-N'-(3-dimethylaminopropyl)carbodiimide (EDC), 2-(N-morpholino) ethanesulfonic acid buffer (MES hydrate, ≥99.5%), potassium hexacyanoferrate(III) ($K_3Fe(CN)_6$, ≥ 99.0%), potassium hexacyanoferrate(II) trihydrate ($K_4Fe(CN)_6.3H_2O$, 98.5–102.0%), human serum were purchased from Sigma Aldrich. Glycerol ($C_3H_8O_3$, anhydrous) and N-hydroxysuccinimide (NHS, >98%) were purchased from Fisher Scientific. Bovine Serum Albumin (BSA, pH 7.0) was purchased from Bio Basic. Artificial human urine was purchased from Biochemazone™. Polyclonal Anti-Apolipoprotein A1 antibody (Anti-APO-A1) and Apolipoprotein A1 (APO-A1) were purchased from Abcam. All solutions were prepared in DI ($\rho = 18.2$ MΩ) unless mentioned otherwise.

2.2. Instrumentation

All electrochemical experiments were carried out using the Autolab PGSTAT204 electrochemical workstation (Metrohm Autolab). The electrochemical cell consisted of a three-electrode system with the screen-printed carbon electrode (SPCE) as the working electrode, platinum wire as the counter electrode and Ag/AgCl (3 M KCl) as the reference electrode. The surface morphology was studied using high resolution transmission electron microscopy (HRTEM, JEOL JEM-3010) and field emission scanning electron microscopy (FESEM, JEOL-6330). Additionally, microdiffraction analysis, energy dispersive spectrometry (EDS), elemental mapping and line profile analysis were performed using a field emission gun transmission electron microscope (FEG-TEM, Tecnai F20 G2 MAT S-TWIN) to confirm the elemental composition of the synthesized Au@AgNWs and the uniformity of the Au layer deposition on the Ag NW surface. Additionally, chemical composition was also studied using high resolution X-ray photoelectron spectroscopy (XPS, JEOL JPS 9030 XPS). Crystallographic analysis was carried out via synchrotron based in situ powder X-ray diffraction at the National Synchrotron Radiation Research Centre (NSRRC). In addition, selected area electron diffraction (SAED, JEOL JEM-3010) and compositional analysis using elemental mapping via energy dispersive X-ray analysis (EDS, X-MAX80T) were also performed.

2.3. Synthesis of AgNWs

AgNWs were prepared using a modified polyol method based on our previous work [22,23]. A typical synthesis protocol involved heating 25 mL of ethylene glycol (EG) in a round bottom flask to 150 °C followed by addition of 30 mL of PVP (0.45 M in EG) and allowed to heat up to 150 °C. 1 mL of $CuCl_2$ (7.3 mM in EG) was then added followed immediately by 10 mL of $AgNO_3$ (0.15 M in EG). The reaction mixture was maintained at 150 °C for 2 h with occasional stirring and was later allowed to cool down to room temperature. AgNWs were collected by centrifuging 3 times in DI water at 3000 rpm for 10 mins followed by redispersion in DI water to reach a final concentration of 0.17 mg/mL.

2.4. Synthesis of Au@AgNWs

The synthesis of Au coated Ag NWs (Au@AgNWs) required the preparation of two separate solutions. Solution 1 (Au growth solution): 2 mL $HAuCl_4$ (1.5 mM), 480 μL NaOH (0.2 M), 6 mL Na_2SO_3 (0.02 M) and 9.44 mL DI were added sequentially in a glass beaker and kept undisturbed for 10 h. Solution 2: 1 mL Ag NWs solution (0.17 mg/mL), 2 mL DI and 3.75 mL ascorbic acid (0.5 M) were added in a glass beaker. The synthesis of Au coated Ag NWs involved the addition of Solution 1 to Solution 2 using a syringe pump at a flow rate of 3 mL/hour for 2.5 h and an additional 1 h under low rpm stirring (<100 rpm) to ensure deposition of a thin layer of Au on the Ag NW surface. The Au@AgNWs were collected by centrifuging 3 times in DI water at 3000 rpm followed by redispersion in DI water (0.05 μg/mL) and stored at 4 °C for later use. The systematic protocol for synthesis of AgNWs and Au@AgNWs is

schematically illustrated in Fig. 1.

2.5. Synthesis of BSA/Au@AgNWs/GA nanocomposite

The BSA/Au@AgNWs/GA nanocomposite was prepared by mixing 1 mL of the synthesized Au@AgNWs solution with 5.0 mg of BSA. The nanocomposite was prepared by mixing aliquots of the BSA/Au@AgNWs mixture with varying amounts of 25% Glutaraldehyde (GA) as shown in Table 1. GA was added to initiate cross linking and produce a nanocomposite containing Au@AgNWs embedded in a 3D BSA matrix.

2.6. Development of immunosensor for APO-A1 detection

2.6.1. Fabrication of SPCE

The SPCE was fabricated using screen-printing of nanomaterial-based carbon paste on flexible PET substrates and the process was low cost and scalable. The screen-printed single-working electrode (Ø = 4 mm) was cured in a vacuum oven at 130 °C for 30 min to improve the electrical and mechanical properties and ensure improved adhesion with the PET substrate.

2.6.2. Optimization and characterization of the 3D nanocomposite coating

The optimum concentration of the 3D BSAu@AgNW/GA nanocomposite coating used to modify the SPCE was determined by two methods. Firstly, the morphology of the bare electrode and the three different modified electrodes (SPCE/BSA/Au@AgNWs/GA-1, SPCE/BSA/Au@AgNWs/GA-3 and SPCE/BSA/Au@AgNWs/GA-5) were studied using top and cross-sectional SEM to evaluate uniformity of the coating, the extent of crosslinking, the porosity of the BSA matrix and the presence of Au@AgNWs. Secondly, all three modified electrodes were electrochemically characterized to examine the electron transfer behavior using Electrochemical impedance spectroscopy (EIS) in 5 mM $[Fe(CN)_6]^{+2}/[Fe(CN)_6]^{+3}$ with an applied frequency range of 0.01 Hz to 100 kHz and an amplitude of 5 mV. EIS is a non-destructive technique which can sensitively monitor the changes at the electrode/solution interface. The diameter of the semi-circle in the Nyquist plot can be utilized to determine the resistance to charge transfer (R_{ct}). The optimum electrode is expected to possess a rough and porous 3D BSA matrix with highly conductive ultra-long Au@AgNWs channeling outward through the pores and a reasonably low overall R_{ct} value. These two parameters will ensure the development of a conductive modified electrode with high electroactive surface area capable of effective antibody immobilization and hence reliable and sensitive immunosensing.

Table 1
Specific concentrations of the BSA/Au@AgNWs and 25% GA used for the nanocomposite preparation.

Sample name	Amount of BSA/Au@AgNWs (μL)	Amount of 25% GA (μL)	Ratio BSA/GA (μg/μL)	Total Volume (μL)
BSA/Au@AgNWs/GA-1	69	1	0.345:1	70
BSA/Au@AgNWs/GA-3	67	3	0.335:3	70
BSA/Au@AgNWs/GA-5	65	5	0.325:5	70

Additionally, the 3D nanocomposite modified SPCE fabricated under the optimized conditions was subjected to further electrochemical characterizations using cyclic voltammetry (CV) in 5 mM $[Fe(CN)_6]^{+2}/[Fe(CN)_6]^{+3}$ with varying scan rates. The voltammograms recorded at different scan rates provided valuable insights on the electron transfer and diffusion profiles of the electroactive species at the electrode surface modified with the nanocomposite coating.

2.6.3. Antifouling capability of the 3D nanocomposite coating

The antifouling capability of the optimized 3D nanocomposite coating was tested using cyclic voltammetry by subjecting the modified electrode to incubation in various complex fluids like 1% BSA, human serum and artificial urine for a time period of 1 h, 1 day, 1 week and 1 month. A minimal decrease in the magnitude of the peak current after an

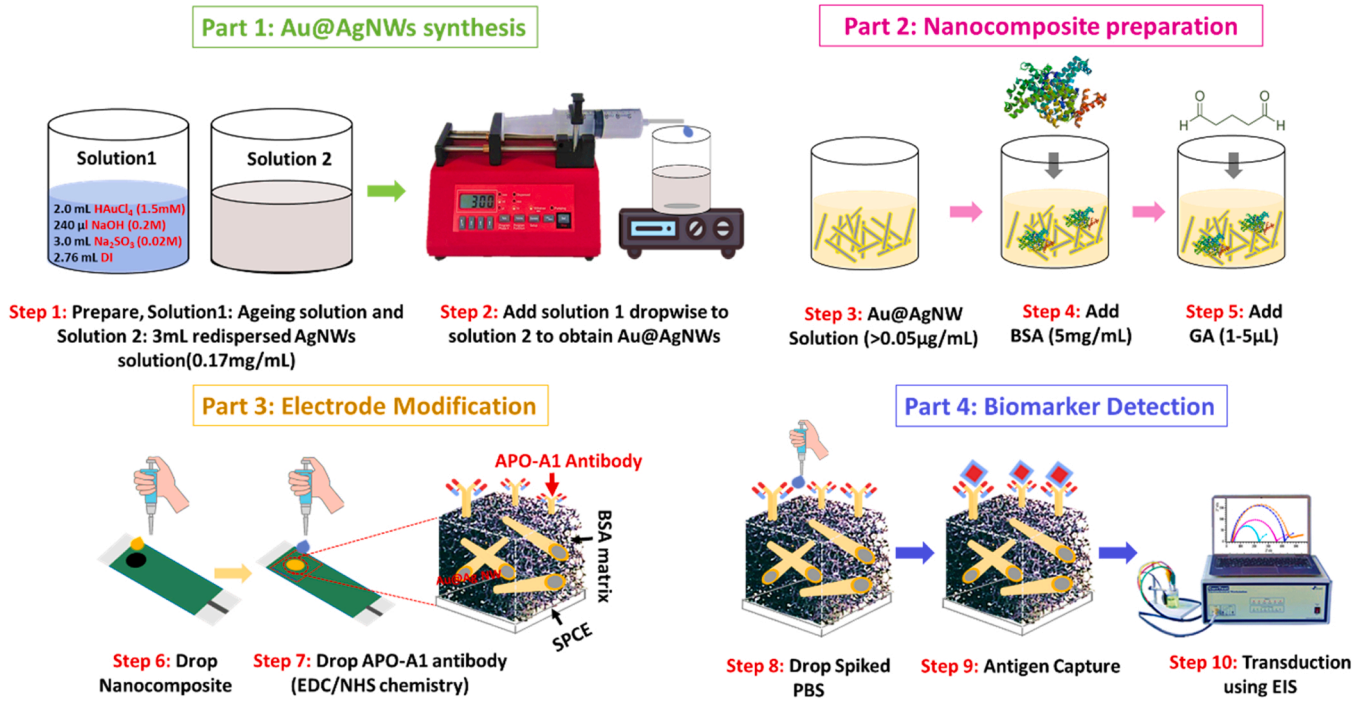

Fig. 1. Schematic representation of the systematic protocol for Au@AgNWs synthesis, nanocomposite preparation, fabrication of the modified electrode and finally the biomarker detection using EIS.

extended incubation period in these complex fluids (relative to the peak current recorded for fresh coatings) would be an accurate parameter to demonstrate the antifouling capabilities of the 3D nanocomposite coating. Additionally, a control test using the bare SPCE incubated in 1% BSA for 1 h, 1 day, 1 week and 1 month was also performed to verify biofouling which takes place in the absence of the 3D nanocomposite coating.

2.6.4. Fabrication and testing of immunosensor

The complete steps for nanocomposite synthesis, electrode modification and immunosensor operation are schematically illustrated in Fig. 1. The SPCE was first modified by drop casting the optimized 3D BSA/Au@AgNWs/GA nanocomposite coating. The electrode was then maintained in a water saturated chamber for 24 h at room temperature. After the coating had completely dried, APO-A1 antibody was immobilized on the electrode surface using EDC/NHS chemistry. Typically, each SPCE/BSA/Au@AgNWs/GA electrode was incubated with 400 mM N-ethyl-N'-(3-dimethylaminopropyl) carbodiimide (EDC) and 200 mM N-hydroxysuccinimide (NHS) in 0.1 M 2-(N-morpholino) ethanesulfonic acid buffer (MES, pH 6.0) for 30 min, rinsed with DI water and dried. Finally, 10 μL of APO-A1 antibody (200 μg/mL, 0.5% glycerol in PBS at 7.4 pH) was dropped and maintained at 4 °C for 10 h. The electrode was then rinsed with DI water and dried. The modified SPCE/BSA/Au@AgNWs/GA/Anti-APO-A1 can now be used directly or

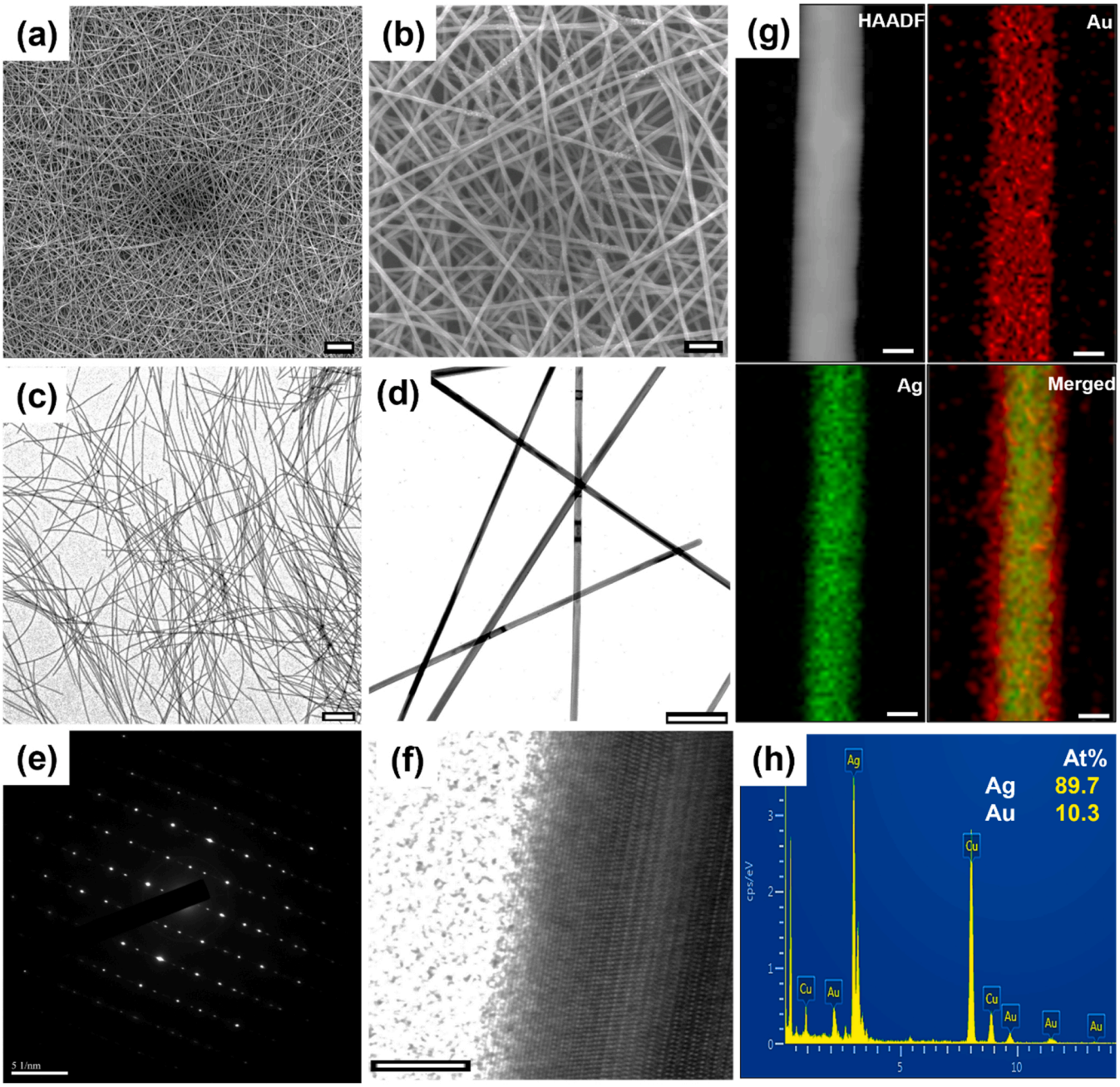

Fig. 2. (a, c) SEM and TEM images of the synthesized Ag NWs with high aspect ratio and uniform diameter [Scale bar = 1 μm]. (b, d) SEM and TEM images of the synthesized Au@AgNWs with a uniform and smooth surface indicating an efficient epitaxial growth of the Au layer on the Ag core [Scale bar = 200 nm]. (e) SAED pattern of the synthesized Ag nanowires. (f) HRTEM image showing the lattice fringes of the synthesized Ag nanowires. (g) EDS elemental analysis of the Au@AgNWs wherein the elemental composition comprising of Au (red) and Ag (green) can be observed [Scale bar = 20 nm]. (h) EDS analysis of Au@AgNWs showing an overall Au weight percentage of 10.3%.

stored at 4 °C for further use. The entire fabrication process of the immunosensor and the recognition of the analyte was monitored using EIS.

The feasibility of the fabricated immunosensor for APO-A1 detection was tested in spiked PBS buffer solution. EIS measurements were performed in 5Mm $[Fe(CN)_6]^{+2}/[Fe(CN)_6]^{+3}$/2 mM PBS using an applied frequency range of 0.01 Hz to 100 kHz and an amplitude of 5 mV with SPCE/BSA/Au@AgNWs/GA/Anti-APO-A1 as the working electrode, Pt as the counter electrode and Ag/AgCl as the reference electrode. The impedance value before immunosensing was noted from the resultant Bode plot and is denoted as Z_o. Subsequently, immunosensing using aliquots of spiked PBS buffer containing APO-A1 protein with concentrations of 100 pg/mL, 10 ng/mL, 50 ng/mL, 75 ng/mL, 100 ng/mL, 150 ng/mL, 175 ng/mL, 200 ng/mL and 250 ng/mL was performed and the resultant Z values were noted. The immunosensor response was measured by normalizing the impedance change observed during immunosensing $[\triangle Z = Z(\text{after } \textit{immunosensing}) - Zo(\text{after antibody } \textit{immobilization})]$ with the impedance observed after antibody immobilization $[Z(\text{after antibody } \textit{immobilization})]$ as shown below:

$$\text{Normalized immunosensor } \textit{response} = \frac{\triangle Z(\text{During } \textit{immunosensing})}{Zo(\text{After antibody } \textit{immobilization})}$$

The use of a normalized immunosensor response eliminates the differences between initial resistance of each electrode and ensures a reliable response during immunosensing. Finally, the immunosensor response to different concentrations of APO-A1 was used to plot the calibration curve and obtain sensitivity and limit of detection (LOD). Five different immunosensors were tested for each concentration of APO-A1 to ensure sensor-to-sensor reproducibility. Furthermore, specificity tests were performed in the presence of interfering proteins that may be present in urine like human serum albumin (HSA) and actin and overexpressed in BC patients like IL-8.

3. Results and discussion

3.1. Characterization of the synthesized Ag NWs and Au@AgNWs

The polyol method shown in Fig. 1 resulted in the successful synthesis of ultra-long Ag NWs with high aspect ratio. The morphology of the synthesized Ag NWs was investigated using TEM and SEM as shown in Fig. 2. The Ag NWs exhibited uniform diameter and a nanowire length of over 100 μm as shown in the SEM images. The Ag NWs were then coated with a uniformly thin Au layer using an epitaxial growth mechanism. It is worth mentioning that galvanic replacement between $Au^{+2/+3}$ and metallic Ag must be strictly avoided to ensure smooth and overall uniform deposition of the Au layer[24]. Galvanic replacement was effectively eliminated by using the ageing solution containing $HAuCl_4$, and Na_2SO_3 which resulted in the formation of a highly stable Au $(SO_3)_2^{2-}$ complex (pK_{sp} of −26.8) that has a lower reduction potential (E^o=0.111 V) than that of Ag^+ (E^o =0.8 V)[25]. Au and Ag have a very small lattice mismatch (4%), thus making it possible to achieve epitaxial deposition of a smooth and uniformly thin conformal coating of Au on the Ag NW surface [23]. Additionally, the reaction time and Au to sulfite ratio is vital to achieving uniform epitaxial growth of Au on the surface of Ag NWs. Varying these two parameters can effectively control the extent and thus the thickness of the deposited Au layer[26]. For this study, a uniformly thin Au layer on the Ag NWs surface is ideal as the high aspect ratio of Ag nanowires confers improved conductivity while the inert gold shell ensures that the nanowires are biocompatible and resistant to oxidation. The optimum condition was achieved at 2 mL of 1.5 mM $HAuCl_4$ and 3 mL of 0.02 M Na_2SO_3 which translated to an overall epitaxial Au deposition of 20.3% (atomic weight). The thin and uniform Au layer over the Ag core was successfully observed using EDS elemental mapping analysis as presented in Fig. 2(g). Moreover, the crystallinity of the synthesized AgNWs and Au@AgNWs was studied using synchrotron based in situ X-ray diffraction at 25 °C. The major peaks corresponding to (111), (200) and (220) of Au and Ag were indexed indicating good crystallinity of the synthesized AgNWs and Au@AgNWs as shown in supplementary Fig. 1. Additionally, the XPS spectra in supplementary Fig. 2 shows the characteristic peaks of Ag $3d_{3/2}$ (368.15 eV) and Ag $3d_{5/2}$ (347.05 eV) and the peaks at 83.08 eV and 87.81 eV are attributed to Au 4 $f_{5/2}$ and Au 4 $f_{7/2}$. This confirms the presence of both Ag and Au in its metallic form in the synthesized Au@AgNWs [27,28].

3.2. Morphology of the 3D nanocomposite coating

The bare SPCE was modified using three different nanocomposite coatings consisting of varying amounts of BSA/Au@AgNWs and 25% GA. The surface morphology of the modified electrodes designated as SPCE/BSA/Au@AgNWs/GA-1, SPCE/BSA/Au@AgNWs/GA-3 and SPCE/BSA/Au@AgNWs/GA-5 containing 1 μL, 3 μL and 5 μL of 25% GA, respectively, were investigated using SEM and the corresponding images are shown in Fig. 3. An obvious difference in the surface morphology of the bare SPCE (Fig. 3a) in comparison to that of the nanocomposite modified SPCE was observed. Furthermore, the difference in the amount of GA (which acts as a crosslinker) and BSA/Au@AgNWs mixture in the nanocomposite coatings resulted in an overall difference in the porosity and thus the roughness of the modified electrodes. SPCE/BSA/Au@AgNWs/GA-1 (Fig. 3b) with the lowest GA concentration was observed to have a relatively smooth surface due to limited crosslinking and the Au@AgNWs could be seen enveloped completely within the BSA with only very few protruding outwards. Fig. 3(c) and (d) show the surface morphology of the SPCE/BSA/Au@AgNWs/GA-3 and SPCE/BSA/Au@AgNWs/GA-5, respectively. Both of these modified electrodes exhibited a rough and porous surface structure with Au@AgNWs visibly embedded in the BSA matrix and also appearing to be channeling outward through the pores. This increased surface roughness is invariably due to the increase in GA concentration which effectively increased the crosslinking[29,30]. In inference to the SEM images, SPCE/BSA/Au@AgNWs/GA-3 and SPCE/BSA/Au@AgNWs/GA-5 which exhibited rough surfaces due to a porous BSA matrix with exposed Au@AgNWs are expected to show superior electrochemical properties in comparison to SPCE/BSA/Au@AgNWs/GA-1 which appeared to have a smooth surface and limited Au@AgNWs exposed on the surface. It is imperative that this increase in crosslinking also essentially increased the thickness of the BSA matrix. This difference in thickness, in addition to the positioning of the Au@AgNWs within the BSA matrix, will translate to distinct characteristic electrochemical behavior due to differences in the double layer capacitance (C_{dl}) and resistance to charge transfer (R_{ct})[31]. Hence it is crucial to determine the optimum conditions to fabricate the modified electrodes. Although the surface morphology from the SEM analysis predicts superior performance of SPCE/BSA/Au@AgNWs/GA-3 and SPCE/BSA/Au@AgNWs/GA-5, confirmatory electrochemical testing was performed to support the interpretation as discussed in the section ahead.

3.3. Electrochemical behavior of the 3D nanocomposite coating

To determine the optimum fabrication conditions which translates to improved electrochemical performance, the electron transfer behavior of the bare and three modified electrodes (SPCE/BSA/Au@AgNWs/GA-1, SPCE/BSA/Au@AgNWs/GA-3 and SPCE/BSA/Au@AgNWs/GA-5) was studied using EIS in 5Mm $[Fe(CN)_6]^{+2}/[Fe(CN)_6]^{+3}$ and the corresponding Nyquist plots are shown in Fig. 4(b). The diameter of the semi-circle (corresponding to the observed R_{ct}) was examined and found to be lowest for the bare SPCE while increasing sequentially with higher GA concentrations. This increase in R_{ct} also signifies greater crosslinking which results in an increased overall dielectric behavior of the modified electrode[32,33]. In addition, the increased thickness of the cross-linked nanocomposite owing to higher GA concentrations further hinders the

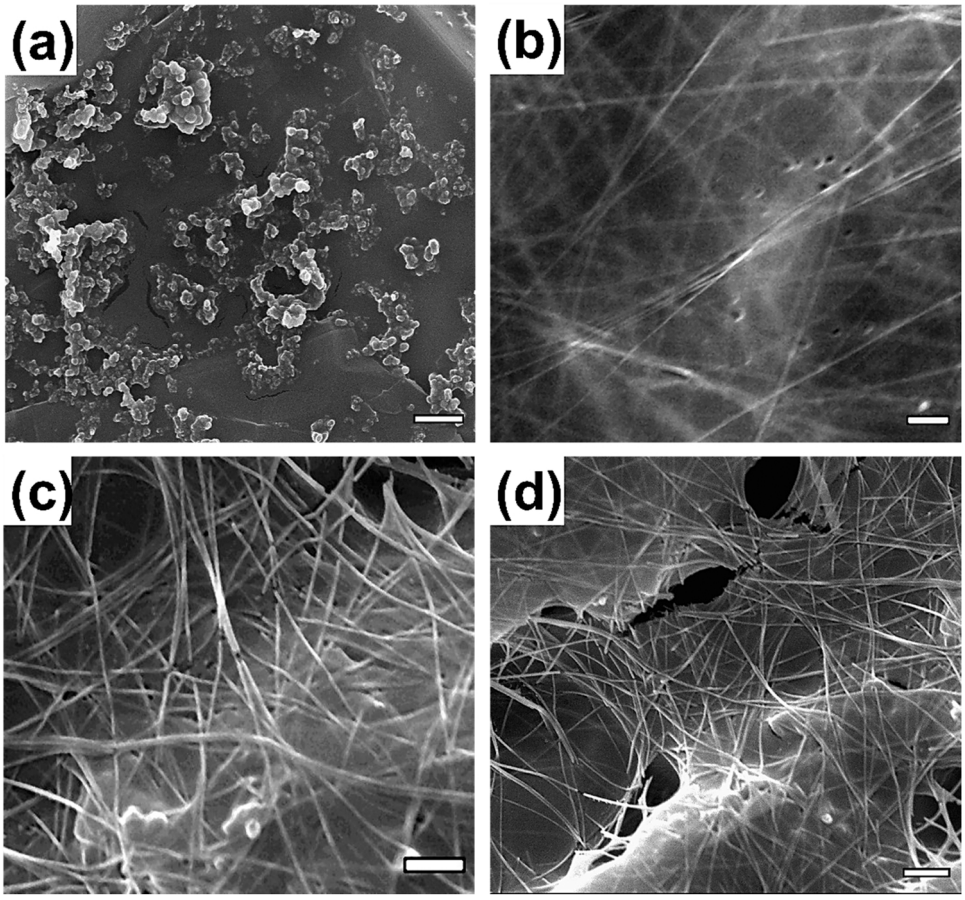

Fig. 3. SEM images of (a) Bare SPCE, (b) SPCE/BSA/Au@AgNWs/GA-1, (c) SPCE/BSA/Au@AgNWs/GA-3 and (d) SPCE/BSA/Au@AgNWs/GA-5. [Scale bar = 500 nm].

electron transfer kinetics. This variation in R_{ct} values of the different nanocomposite coatings is in accordance with the surface morphology observed in the SEM images shown in Fig. 3 which clearly depicted an increase in surface roughness and porosity with higher GA concentrations. The SPCE/BSA/Au@AgNWs/GA-3 showed excellent porosity and surface roughness with exposed Au@AgNWs channeling through the pores as compared to SPCE/BSA/Au@AgNWs/GA-1 while also exhibiting a significantly smaller R_{ct} value as compared to SPCE/BSA/Au@AgNWs/GA-5. Additionally, SPCE/BSA/Au@AgNWs/GA-3 with five different Au@AgNWs concentrations (0 μg/mL, 0.025 μg/mL, 0.050 μg/mL, 0.075 μg/mL, and 0.100 μg/mL) was prepared and subjected to EIS and CV investigations. The corresponding Nyquist plots and cyclic voltammograms are shown in supplementary Fig 3. An increase in peak current and lowering in R_{ct} value was observed at lower concentrations of Au@AgNWs (0.025 μg/mL and 0.050 μg/mL), signifying an enhancement in electrochemical behavior as compared to the modified electrode without Au@AgNWs. This can be attributed to the improved charge transfer due to formation of highly conductive Au@AgNWs channels. However, further increase in concentrations of Au@AgNWs (0.075 μg/mL and 0.100 μg/mL) resulted in a diminished peak current and large R_{ct} value, which is presumably due to blocking of the pores in the 3D nanocomposite matrix due to extensive population of the Au@AgNWs. Conclusively, the highest peak current and lowest R_{ct} value was observed at an Au@AgNWs concentration of 0.05 μg/mL. Hence, SPCE/BSA/Au@AgNWs/GA-3 containing 0.05 μg/mL of Au@AgNWs was chosen as the optimized working electrode.

This optimized electrode was subjected to further electrochemical testing to determine the transport behavior of electro active species at the electrode/solution interface. Given the morphology of SPCE/BSA/Au@AgNWs/GA-3, we hypothesize that the BSA matrix passivates the electrode surface while charge transfer between the electro-active species in solution and the modified electrode can arise due to the exposed Au@AgNWs channeling though the pores[33,34]. To further investigate this hypothesis, cyclic voltammetry (CV) was performed using SPCE/BSA/Au@AgNWs/GA-3 as the working electrode in 5 mM $[Fe(CN)_6]^{+2}/[Fe(CN)_6]^{+3}$ at different scan rates (0.07–0.1 mVs^{-1}) and the resulting voltammograms are shown in Fig. 4(e). Typical transient voltammograms were observed at lower scan rates (wherein the electro-active species inherently follow a radial diffusion profile) which is indicative of overlapped diffusion profiles of numerous Au@AgNWs in adjacent pores as the distance of diffused electro active species surpasses the pore size. Consequently, at higher scan rates (wherein the electro active species follow a linear diffusion profile), sigmoidal voltammograms were observed in which the observed current is the overall contributed effect of the diffusions at all the pores (channeled with Au@AgNWs acting as multiple independent nanoelectrodes). The existence of two distinct voltammograms at lower and higher scan rates reveals the dependence of the overall electrochemical behavior of the modified electrode on the surface roughness/porosity of the 3D BSA matrix and the presence of the conductive Au@AgNWs within the pores.

3.4. Antifouling capability and immunosensor performance

To ensure reliability for detection in complex fluids, the antifouling capability of the 3D nanocomposite coating was tested by incubating in 1% BSA, human serum and artificial urine. As shown in Fig. 5(a), the bare SPCE showed a 100% decrease in peak current after just 1 h of incubation in 1% BSA and hence further investigation in human serum and artificial urine was dismissed. However, the SPCE/BSA/Au@AgNWs/GA-3 showed a minimal loss (~12%) in peak current

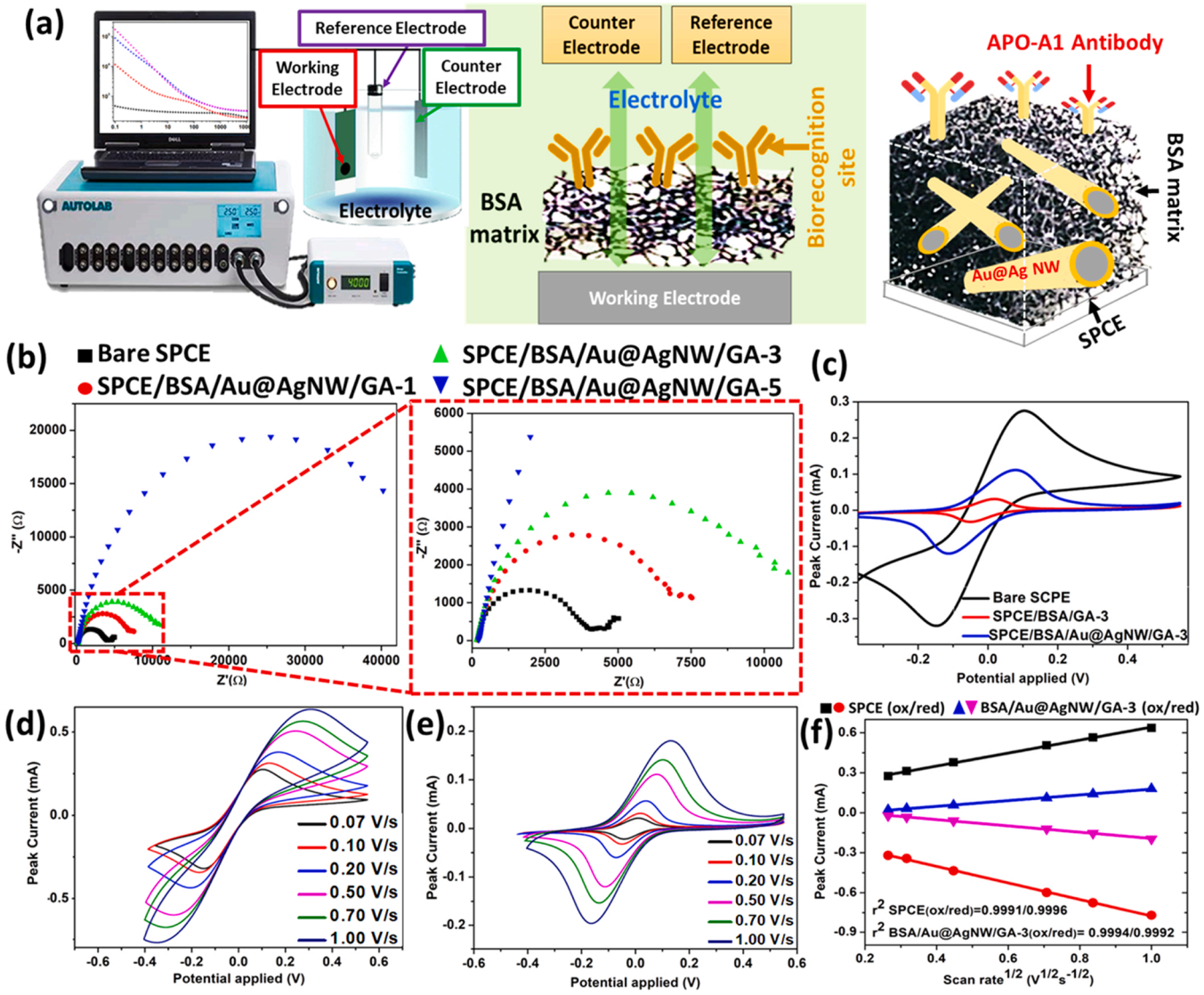

Fig. 4. (a) (Left to right) Schematic representations of the electrochemical setup utilized for the characterization of the 3D nanocomposite modified SPCE and the fabricated immunosensor. (b) Nyquist plot of the bare and modified SPCE showcasing an increasing in R_{ct} values with increasing amount of GA in the nanocomposite. The SPCE/BSA/Au@AgNWs/GA-3 was found to be the optimized electrode and was subjected to further electrochemical testing. (c) Typical voltammograms showing oxidation and reduction peaks of bare SPCE, SPCE/BSA/GA-3 and in 5 mM $[Fe(CN)_6]^{+2}/[Fe(CN)_6]^{+3}$. (d) Voltammograms of bare SPCE and (e) SCPE/BSA/Au@AgNWs/GA-3 in 5 mM $[Fe(CN)_6]^{+2}/[Fe(CN)_6]^{+3}$ at different scan rates (0.07–1.0 Vs^{-1}). (f) Extracted oxidation/reduction peak current (*ip*) from the voltammograms shown in (d) and (e) plotted versus the square root of the scan rate.

after 1 month of incubation which establishes the excellent antifouling capability and robust storage stability of the 3D nanocomposite modified electrodes. This observed antifouling behavior could be attributed to two major reasons (i) size exclusion due to extensive porosity imparted by the efficient crosslinking of BSA using GA which creates a sieve like matrix and blocks the access of interferents to the electrode surface [33] in addition to the BSA matrix (isoelectric point= 4.7) based charge repulsion at physiological pH, which repels soluble proteins such as albumin and (ii) the highly biocompatible and chemically inert Au coating which uniformly sheaths the AgNWs, thereby maintaining stable and highly conductive channels in the BSA matrix by eliminating any possible oxidation of the Ag core.

Subsequently, the SPCE/BSA/Au@AgNWs/GA was subjected to EDC/NHS chemistry to successfully immobilize APO-A1 antibodies covalently to the 3D BSA matrix. The resulting SPCE/BSA/Au@AgNWs/GA-3/Anti-APO-A1 was utilized as the working electrode for immunosensing of different concentrations of BC protein biomarker APO-A1 (100 pg/mL, 1 ng/mL, 10 ng/mL, and 250 ng/mL). The immunosensor response was observed using EIS and the resulting Nyquist and Bode plots are shown in Fig. 5(b). Each APO-A1 concentration was analysed using 5 individual immunosensors to ensure reliable and reproducible results. Finally, the normalized impedance variation (calculated as ΔZ/Z %) was extracted from the resultant Bode plots and chosen as the appropriate method to express the immunosensor response to analyte concentration as shown in Fig. 5(c). The fabricated immunosensor exhibited excellent sensitivity for APO-A1 detection in the sensing range of 100 pg/mL to 250 ng/mL with a calculated limit of detection (LOD) of 22.03 pg/mL (calculated as LOD=3.3 x standard deviation of the regression line (σ)/Slope) and demonstrated high reproducibility (n = 5, RSD=2.2%) as indicated by the small error bars in Fig. 5(c). The specificity of the immunosensor towards APO-A1 was also investigated against interfering proteins that may be present in urine like human serum albumin (HSA) and actin and overexpressed in BC patients like Il-8. The minimal normalized impedance variation observed for 250 ng/mL of HSA (2.4%), actin (3.3%) and IL-8 (4.2%) in comparison to APO-A1 (93.3%) confirms the outstanding specificity of the immunosensor

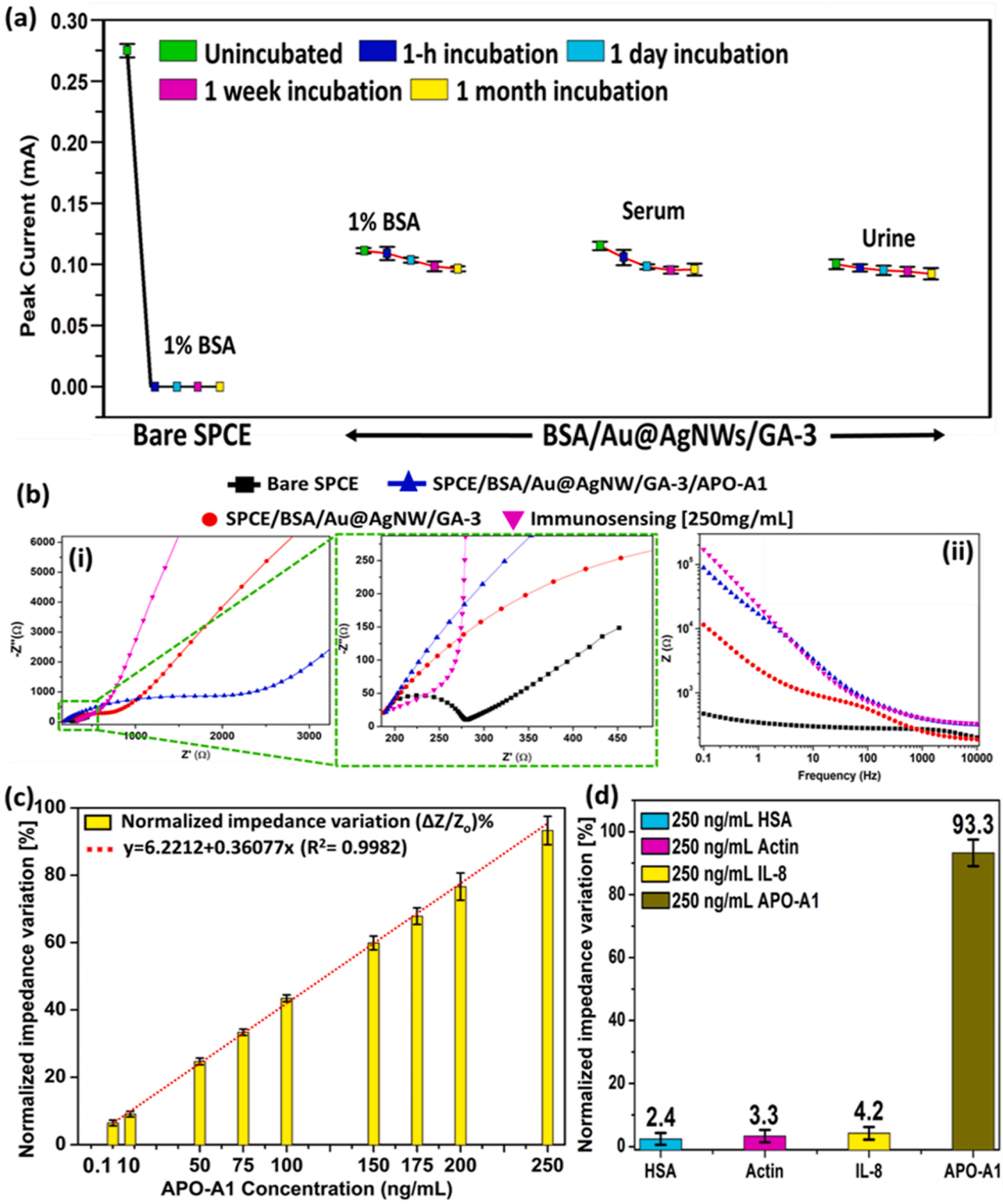

Fig. 5. (a) Demonstration of the excellent antifouling capabilities of the 3D nanocomposite coating after incubation in 1% BSA, human serum and artificial urine for up to 1 month. (b) (i) Nyquist plot (enclosed in green is the magnified view of the Nyquist plot) and (ii) Bode plot during each step of the SPCE modification process leading up to the immunosensing of 250 ng/mL APO-A1. (c) The immunosensor response observed for different APO-A1 concentrations (n = 5). (d) Specificity tests showing the immunosensor response against major interfering proteins such as human serum albumin (HSA), actin and interleukin (IL-8) in comparison to APO-A1 (n = 5). [Error bars in all graphs represent the s.d of the mean].

(Fig. 5d). Consequently, the proposed immunosensor utilizing the 3D nanocomposite modified SPCE demonstrated excellent analytical performance for the quantification of BC protein biomarker APO-A1. These results highlight the potential of this immunosensing platform for the sensitive detection of any protein biomarker of choice by simply immobilizing the appropriate antibody during fabrication.

4. Conclusion

In summary, we have synthesized ultra-long AgNWs with high aspect ratio and utilized a sulfite mediated protocol to epitaxially deposit a smooth and uniform coating of Au on the surface of the AgNWs (Au@AgNWs). The as synthesized Au@AgNWs were incorporated with optimized amounts of BSA and GA (crosslinking agent) to develop a novel 3D nanocomposite coating on the SPCE. This nanocomposite coating consisted of a network of highly conductive and biocompatible Au@AgNWs embedded within the 3D porous BSA matrix which enables oriented antibody immobilization and exhibits excellent antifouling capability. Finally, using the optimized 3D nanocomposite modified SPCE, we fabricated an immunosensor for detection of BC protein biomarker APO-A1. This low cost immunosensor demonstrated a high sensitivity for APO-A1 in the sensing range of 100 pg/mL to 250 ng/mL with an impressive LOD of 22.03 pg/mL in spiked buffer. Furthermore, the developed immunosensor exhibited outstanding specificity for APO-A1 detection with a minimal response observed against interfering proteins like HSA, actin and IL-8. These results further highlight the potential of this platform technology for the sensitive and specific immunosensing of any protein biomarker of choice.

CRediT authorship contribution statement

R. K. Rakesh Kumar: Methodology, Investigation, Visualization, Writing – original draft; **Amit Kumar:** Methodology, Investigation, Visualization, Writing – original draft; **Cheng-Hsin Chuang:** Validation, Writing – reviewi & editing, Supervision; **Muhammad Omar Shaikh:** Conceptualization, Supervision, Project administration, Funding acquisition.

Declaration of Competing Interest

The authors declare that they have no known competing financial interests or personal relationships that could have appeared to influence the work reported in this paper.

Data Availability

Data will be made available on request.

Acknowledgements

The authors would like to thank the Ministry of Science and Technology, Taiwan, for financially supporting this research under Contract No. 111-2222-E-029-001-MY3.

Appendix A. Supporting information

Supplementary data associated with this article can be found in the online version at doi:10.1016/j.snb.2023.133621.

References

[1] A. Richters, K.K. Aben, L.A. Kiemeney, The global burden of urinary bladder cancer: an update, World J. Urol. 38 (2020) 1895–1904.
[2] A.M. Kamat, N.M. Hahn, J.A. Efstathiou, S.P. Lerner, P.-U. Malmström, W. Choi, et al., Bladder cancer, Lancet 388 (2016) 2796–2810.
[3] C. Yeung, T. Dinh, J. Lee, The health economics of bladder cancer: an updated review of the published literature, Pharmacoeconomics 32 (2014) 1093–1104.
[4] M.A. Knowles, C.D. Hurst, Molecular biology of bladder cancer: new insights into pathogenesis and clinical diversity, Nat. Rev. Cancer 15 (2015) 25–41.
[5] S.S. Chang, S.A. Boorjian, R. Chou, P.E. Clark, S. Daneshmand, B.R. Konety, et al., Diagnosis and treatment of non-muscle invasive bladder cancer: AUA/SUO guideline, J. Urol. 196 (2016) 1021–1029.
[6] M. Hong, G. He, S. Goh, A.W.X. Low, K.J. Tay, T.K.H. Lim, et al., Biomarkers for precision urothelial carcinoma diagnosis: Current approaches and the application of single-cell technologies, Cancers 13 (2021) 260.
[7] R.J. Sylvester, O. Rodríguez, V. Hernández, D. Turturica, L. Bauerová, H.M. Bruins, et al., European Association of Urology (EAU) prognostic factor risk groups for non–muscle-invasive bladder cancer (NMIBC) incorporating the WHO 2004/2016 and WHO 1973 classification systems for grade: an update from the EAU NMIBC Guidelines Panel, Eur. Urol. 79 (2021) 480–488.
[8] Z. Wang, H. Que, C. Suo, Z. Han, J. Tao, Z. Huang, et al., Evaluation of the NMP22 BladderChek test for detecting bladder cancer: a systematic review and meta-analysis, Oncotarget 8 (2017), 100648.
[9] H. He, C. Han, L. Hao, G. Zang, ImmunoCyt test compared to cytology in the diagnosis of bladder cancer: A meta-analysis, Oncol. Lett. 12 (2016) 83–88.
[10] R. Chou, C. Cuevas, R. Fu, B. Devine, N. Wasson, A. Ginsburg, Erratum: Imaging techniques for the diagnosis of hepatocellular carcinoma. A systematic review and meta-analysis (Annals of Internal Medicine (2015) 162 (697-711, Ann. Intern. Med. 162 (2015) 880.
[11] A. Anandapadmanabhan, Sensing Devices for Illicit Drug Detection 2017.
[12] D. Wu, Y. Wang, Y. Zhang, H. Ma, T. Yan, B. Du, et al., Sensitive electrochemical immunosensor for detection of nuclear matrix protein-22 based on NH2-SAPO-34 supported Pd/Co nanoparticles, Sci. Rep. 6 (2016) 1–8.
[13] H.O. Othman, F. Salehnia, N. Fakhri, R. Hassan, M. Hosseini, A. Faizullah, et al., A highly sensitive fluorescent immunosensor for sensitive detection of nuclear matrix protein 22 as biomarker for early stage diagnosis of bladder cancer, RSC Adv. 10 (2020) 28865–28871.
[14] C.-H. Chuang, Y.-C. Du, T.-F. Wu, C.-H. Chen, D.-H. Lee, S.-M. Chen, et al., Immunosensor for the ultrasensitive and quantitative detection of bladder cancer in point of care testing, Biosens. Bioelectron. 84 (2016) 126–132.
[15] M.O. Shaikh, T.-C. Huang, T.-F. Wu, C.-H. Chuang, Label free Impedimetric Immunosensor for effective bladder Cancer detection in clinical urine samples, Biomed. Micro 22 (2020) 1–8.
[16] H. Ma, X. Zhang, X. Li, R. Li, B. Du, Q. Wei, Electrochemical immunosensor for detecting typical bladder cancer biomarker based on reduced graphene oxide–tetraethylene pentamine and trimetallic AuPdPt nanoparticles, Talanta 143 (2015) 77–82.
[17] G. Manasa, R.J. Mascarenhas, S.J. Malode, N.P. Shetti, Graphene-based electrochemical immunosensors for early detection of oncomarker carcinoembryonic antigen, Biosens. Bioelectron. X (2022), 100189.
[18] R.R. Kumar, M.O. Shaikh, C.-H. Chuang, A review of recent advances in non-enzymatic electrochemical creatinine biosensing, Anal. Chim. Acta 1183 (2021), 338748.
[19] F. Soria, M.J. Droller, Y. Lotan, P. Gontero, D. D'Andrea, K.M. Gust, et al., An up-to-date catalog of available urinary biomarkers for the surveillance of non-muscle invasive bladder cancer, World J. Urol. 36 (2018) 1981–1995.
[20] A. Chakraborty, S. Dasari, W. Long, C. Mohan, Urine protein biomarkers for the detection, surveillance, and treatment response prediction of bladder cancer, Am. J. Cancer Res. 9 (2019) 1104.
[21] W.S. Tan, W.P. Tan, M.-Y. Tan, P. Khetrapal, L. Dong, P. deWinter, et al., Novel urinary biomarkers for the detection of bladder cancer: a systematic review, Cancer Treat. Rev. 69 (2018) 39–52.
[22] A. Kumar, R. Rakesh Kumar, M.O. Shaikh, C.-H. Lu, J.-Y. Yang, H.-L. Chang, et al., Ultrasensitive strain sensor utilizing a AgF–AgNW hybrid nanocomposite for breath monitoring and pulmonary function analysis, ACS Appl. Mater. Interfaces (2022).
[23] A. Kumar, M.O. Shaikh, R.R. Kumar, K. Dutt, C.-T. Pan, C.-H. Chuang, Highly sensitive, flexible and biocompatible temperature sensor utilizing ultra-long Au@AgNW-based polymeric nanocomposites, Nanoscale 14 (2022) 1742–1754.
[24] L. Zhang, Y. Zhang, J. Ahn, X. Wang, D. Qin, Defect-assisted deposition of Au on Ag for the fabrication of core–shell nanocubes with outstanding chemical and thermal stability, Chem. Mater. 31 (2019) 1057–1065.
[25] H. Liu, T. Liu, L. Zhang, L. Han, C. Gao, Y. Yin, Etching-free epitaxial growth of gold on silver nanostructures for high chemical stability and plasmonic activity, Adv. Funct. Mater. 25 (2015) 5435–5443.
[26] Y. Zhu, S. Kim, X. Ma, P. Byrley, N. Yu, Q. Liu, et al., Ultrathin-shell epitaxial Ag@Au core-shell nanowires for high-performance and chemically-stable electronic, optical, and mechanical devices, Nano Res. 14 (2021) 4294–4303.
[27] K.K. Haldar, S. Tanwar, R. Biswas, T. Sen, J. Lahtinen, Noble copper-silver-gold trimetallic nanobowls: An efficient catalyst, J. Colloid Interface Sci. 556 (2019) 140–146.
[28] Y.-C. Wang, M.H. Engelhard, D.R. Baer, D.G. Castner, Quantifying the impact of nanoparticle coatings and nonuniformities on XPS analysis: gold/silver core–shell nanoparticles, Anal. Chem. 88 (2016) 3917–3925.
[29] U. Zupančič, P. Jolly, P. Estrela, D. Moschou, D.E. Ingber, Graphene enabled low-noise surface chemistry for multiplexed sepsis biomarker detection in whole blood, Adv. Funct. Mater. 31 (2021) 2010638.
[30] E. Bronze-Uhle, B. Costa, V. Ximenes, P. Lisboa-Filho, Synthetic nanoparticles of bovine serum albumin with entrapped salicylic acid, Nanotechnol., Sci. Appl. 10 (2017) 11.
[31] A. Rehman, X. Zeng, Interfacial composition, structure, and properties of ionic liquids and conductive polymers for the construction of chemical sensors and biosensors: a perspective, Curr. Opin. Electrochem. 23 (2020) 47–56.

[32] L. Yu, M. Li, Q. Kang, L. Fu, G. Zou, D. Shen, Bovine serum albumin-stabilized silver nanoclusters with anodic electrochemiluminescence peak at 904 nm in aqueous medium and applications in spectrum-resolved multiplexing immunoassay, Biosens. Bioelectron. 176 (2021), 112934.
[33] J. Sabaté del Río, O.Y. Henry, P. Jolly, D.E. Ingber, An antifouling coating that enables affinity-based electrochemical biosensing in complex biological fluids, Nat. Nanotechnol. 14 (2019) 1143–1149.
[34] A. Barfidokht, S. Ciampi, E. Luais, N. Darwish, J.J. Gooding, Distance-dependent electron transfer at passivated electrodes decorated by gold nanoparticles, Anal. Chem. 85 (2013) 1073–1080.

R.K. Rakesh Kumar received his B.Sc. in Physics, Chemistry and Mathematics in 2016 from Christ University, India. He is currently a PhD student at the Institute of Medical Science and Technology in National Sun Yat-sen University, Taiwan, under the supervision of Prof. Cheng-Hsin Chuang. His research interests include nanomaterial synthesis for applications in micro and nano biosensing.

Amit Kumar received his B.Sc. in Physics in 2016 from Delhi University, India. He is currently a PhD student at the Institute of Medical Science and Technology in National Sun Yat-sen University, Taiwan, under the supervision of Prof. Cheng-Hsin Chuang. His research interests include nanomaterials and hybrid nanocomposites for applications in biosensing and smart wearables for human body monitoring.

Dr. Cheng-Hsin Chuang is Chair Professor at the Institute of Medical Science and Technology in National Sun Yat-sen University where he leads the Micro and Nano Sensing Technology (MANST) laboratory. He obtained his B.S. degree and Ph.D. degree from National Cheng Kung University (NCKU) in 1995 and 2002, respectively, both in Civil Engineering. After being a postdoctoral fellow with Centre for Micro/Nano Science and Technology at NCKU and research engineer in the Smart Microsystem Technology Centre at Industrial Technology Research Institute (ITRI), he was appointed to the Department of Mechanical Engineering and Institute of Nanotechnology at Southern Taiwan University of Science and Technology (STUST) during 2005–2018 and promoted to Full Professor and Distinguished Professor in 2013 and 2016, respectively. Currently, his main research interests include smart sensing/actuation technologies, micro/nano electromechanical systems, flexible electronics and AIoT based smart home care.

Dr. Muhammad Omar Shaikh is an Assistant Professor of Sustainability Science and Engineering at Tunghai University. He completed his MEng in Materials Science and Engineering from Imperial College London in 2010 and his Ph.D. in Mechatronic Science and Engineering from the Southern Taiwan University of Science and Technology in 2015. Thereafter, he held two postdoctoral research positions in Taiwan where he conducted highly interdisciplinary research focused on developing micro and nano sensing technologies including biosensors for point-of-care diagnostics, tactile sensors for robotics, gas sensors and wearable energy harvesters for self-powered sensing. He also previously served as the Chief Technology Officer for BiTAPE Logistics, a university spin-off company developing a printed smart tape for providing IoT based logistic services. His current research interests revolve around developing innovative smart sensing/actuation technologies, devising innovative ways to power and communicate with them and utilizing a "system integration" approach to provide holistic solutions for real-world applications.